

# High-Performance Resonant Controller Implemented in the Discrete-Time Domain for Voltage Regulation of Grid-Forming Converters

Zhihong Zhao<sup>✉</sup>, Member, IEEE, Zhichao Sun, Yilong Feng, Baojian Ji<sup>✉</sup>, Shuzheng Wang<sup>✉</sup>, and Jianfeng Zhao<sup>✉</sup>

**Abstract**—Grid-forming converters (GFCs) offering sinusoidal voltage supply have been widely employed in a lot of applications. In this article, the dual-loop voltage–current control for GFCs is comprehensively approached. First, optimum tuning of the current loop is addressed to achieve the maximum enhanced active damping from the prospect of the developed equivalent plant, instead of the current loop, which has been the focus of the existing literature. Then, effectiveness of resonant controllers (RCs), i.e., proportional resonant and vector proportional integral, which are very popular for voltage regulation of GFCs, is addressed. It is found that for GFCs with a reasonably designed output filter, especially for high-power applications with a low switching frequency, a weekly damped region exists in the closed-loop frequency response with either of the two RCs employed, which can further result in constrained bandwidth and slow transient response. To solve this issue, a discrete RC is developed, which avoids the weekly damped region, and a fast response of the output voltage can be achieved. Experimental results have verified the effectiveness of the proposed controller for voltage regulation of GFCs.

**Index Terms**—Active damping, dual-loop control, grid-forming converter (GFC), resonant controller (RC), weekly damped region.

## I. INTRODUCTION

EFFECTIVE sinusoidal voltage regulation is an aspect of paramount importance for grid-forming converters (GFCs) to achieve a high level of performance in a variety of different applications, such as virtual synchronous machine or droop control for grid-tied converters [1]–[3], dynamic voltage restorers [4],

[5], ground power units for airplanes [6], [7], and auxiliary inverters for rail trains [8], [9], to name a few. In these sceneries, GFCs are expected to offer voltage support for the load and/or the grid. It should be mentioned that the term “grid-forming” means the converter presenting a grid characteristic externally, and GFCs can work in both grid-tied and off-grid cases. For instance, for droop control of grid-tied converters, the converter has to first build the voltage (in stand-alone mode with no load) and then connect to the grid with a switch once the phase-locked loop is ready. Alternatively, for ground power units or auxiliary inverters, multiconverters can be connected in parallel working in an autonomous mode, which forms a microgrid with respect to the load. Anyway, the underlying control for both cases is exactly the same, i.e., high-quality and effective voltage control, despite some typical upper layer considerations such as active/reactive power sharing [10], [11], harmonic current sharing [12], [13], increased damping and inertia [14], secondary control for voltage amplitude and frequency restoration [15], etc.

In order to reduce the high-frequency switching ripples, *LC* filters are commonly employed at the output terminal of the converter [16]. However, *LC* filters can cause the stability problem related to resonance, which, in practice, can result in a great challenge to the system’s effective control [6], [8], [9], [16]. Although the resonance phenomenon can be passively damped by adding resistors in series or parallel with the capacitor, this kind of method can, however, bring new issues, such as increased power loss and deteriorated filter effectiveness [6], [16]–[19]. Active damping methods have, therefore, been studied in numerous literature works and considered as a preferable way to solve the issues faced by the passive damping methods stated above.

Currently, the following two types of approaches are commonly employed for active damping of GFCs: 1) single-loop voltage and 2) dual-loop voltage–current control. More specifically, the single-loop voltage control method relies on the intrinsic damping resulted from the one-sampling delay related to digital implementation [6], [16]. This approach is easy to implement since only the capacitor voltage is sensed and fed for regulation. However, it has been proved that this method suffers from the issues of low stability, constrained loop bandwidth, lack of overcurrent protection, and reduced robustness to the parameter detuning of the filter. On the other hand, by introducing the inner current loop to provide enhanced damping to avoid filter

Manuscript received February 5, 2021; revised May 29, 2021 and August 29, 2021; accepted October 10, 2021. Date of publication October 15, 2021; date of current version December 31, 2021. This work was supported in part by the National Natural Science Foundation of China under Project 51807092 and in part by the Open Research Fund of Jiangsu Collaborative Innovation Center for Smart Distribution Network, Nanjing Institute of Technology, under Grant XTCX202004. Recommended for publication by Associate Editor Brendan (GAE) Peter McGrath. (*Corresponding author: Zhihong Zhao.*)

Zhihong Zhao, Zhichao Sun, Yilong Feng, and Baojian Ji are with the Department of Electrical and Engineering, School of Automation, Nanjing University of Science and Technology, Nanjing 210096, China (e-mail: zhaozhihong@njust.edu.cn; sunzhichao0508@163.com; fengyilong@njst.edu.cn; ji\_baojian@126.com).

Shuzheng Wang is with the Jiangsu Province Intelligent Distribution Network Technology and Equipment Collaborative Innovation Center, Nanjing Institute of Technology, Nanjing 210073, China (e-mail: wzs310@126.com).

Jianfeng Zhao is with the Department of Electrical and Engineering, Southeast University, Nanjing 210008, China (e-mail: jianfeng\_zhao@seu.edu.cn).

Color versions of one or more figures in this article are available at <https://doi.org/10.1109/TPEL.2021.3120426>.

Digital Object Identifier 10.1109/TPEL.2021.3120426

resonance, the dual-loop voltage–current control is an effective way to solve the issues faced by the single-loop voltage control method and has, in fact, been approached and implemented in a lot of studies [2], [3], [8], [9], [18], [19].

In these studies, tuning of the current loop has been intensively addressed, where the frequency response analysis is commonly employed. More specifically, the bandwidth of the inner current loop is tuned to be one-tenth to one-fifth of that of the outer voltage loop [3], [6], [8], [9], [18], [19], which is a rule of thumb for dual-loop-regulated applications, for instance, grid-following converters, where the current injected into the grid is concerned [17], [20], [21]. However, according to our findings, this rule is not valid for the case of dual-loop-regulated GFCs. This is because the objective of the current loop is not for signal tracking, but for active damping of the resonance from the filter [6], [8], [9], [16]–[19], [22]. Therefore, the bandwidth is an irrelevant factor for the case of GFCs. Other alternatives include setting the damping of the current loop poles to unity in [19] or 0.707 in [23], where theoretical supports for these claims are, however, insufficient. Also, recently, a kind of hybrid method, which is a combination of the root locus and frequency response analysis, has been developed in [24] for tuning of the current loop. This method searches the current gain, which minimizes the value of the distance between the poles (relating to filter resonance) and the original point in the  $z$ -plane, as long as the acceptable minimum values of phase margin (PM) and gain margin (PM and GM) predefined for stability considerations are both satisfied. However, practically, the standard for the determination of the explicit values of PM and GM is lacking, and their values are, to some extent, depend on the experience and knowledge of the designer. Also, the minimization of the distance between the poles and the original point is not equivalent to the maximization of the active damping of the poles, which will be proved in this article with detailed analytical plots. It should be emphasized that, in recent years, active damping for  $LCL$ -filtered grid-following converters has been intensively investigated by numerous researchers [17], [25], [26], whereas how to design the current loop to offer enhanced active damping for  $LC$ -filtered GFCs has not been fully addressed in the existing studies.

On the other hand, regarding the voltage controller, the scheme based on the proportional–integral (PI) controller implemented in the synchronous reference frame (SRF) rotating with the fundamental frequency  $\omega_e$  is very popular for its easy implementation and has, in fact, been used in a variety of different applications [3], [18]. However, this method has limitations in dealing with the unbalanced and/or nonlinear loads, since the voltages across the filter resulting from the negative sequence (NS) and high-frequency harmonic currents cannot be compensated. Alternatively, the following two types of resonant controllers (RCs) can be employed to obtain a high-quality waveform: 1) proportional–resonant (PR) and 2) vector proportional integral (VPI) [6], [8], [9], [16], [19], [27]–[29]. It has been proved that VPI is superior to PR in terms of stability, disturbance rejection, and robustness to parameter detuning [8], [29]. This conclusion is, however, only valid for the cases of  $L$ -filtered or  $LCL$ -filtered grid-following converters (for frequencies below

the resonant frequency of the  $LCL$  filter), which can be modeled as  $1/(sL + R_L)$  approximately [29], [30]. Also, the R controller (i.e., PR with a zero proportional gain) is employed in [24], since the proportional gain can result in the reduction of GM, and the similar method to that of tuning the current loop is employed for tuning of the voltage loop. Hence, the issue of uncertainty for the values of PM and GM can still be valid in this case. Additionally, it has been proved in [29] that neither PM nor GM can be employed for stability evaluation of the system with multiple 0-dB crossings in the frequency response; therefore, special care should be taken for cases in which RCs are employed, since RCs can always exhibit this kind of complex frequency response. Besides, repetitive controllers, whose frequency response resembles multiple parallel-connected RCs tuned at different frequencies, can also be employed for voltage regulation of GFCs [31], [32]. Also, comparing RCs, repetitive controllers can save the computation resources remarkably. However, RCs have the following benefits with respect to repetitive controllers: 1) more flexible in excitation frequency selection, which means that the designer can tune the RCs at the frequencies of interest conveniently and 2) the stability requirements are easier to meet, since the delay compensation for each RCs can be tuned independently.

With regard to GFCs, the cutoff frequency of the  $LC$  filter can be very low in order to achieve a good cancellation of the high-frequency voltages (especially the switching frequency voltage). Also, a large value of capacitor is commonly employed for the filter, since the cost of the capacitor is much lower compared to that of the inductor, especially for high-power applications. Therefore, in this case, the exceptional performance of VPI mentioned above can be much deteriorated, which should be investigated to avoid unintentional usage. In this article, the effectiveness of both PR and VPI for voltage regulation of GFCs has been thoroughly addressed, which has not been covered by the existing literature.

Alternatively, for a typical application, new controllers can be developed to achieve high performance. The study in [33] and [34] proposed discrete controllers for voltage regulation of GFCs through pole/zero placement to obtain a fast response. However, these controllers have limitations in dealing with the unbalanced and nonlinear loads, since they are developed in the stationary reference frame directly. On the other hand, the continuous- and discrete-time version of a complex proportional–integral (cPI) controller for  $L$ -filtered grid-following converters was developed in [30] and [35], respectively, and has been comprehensively investigated by a lot of researchers since then, such as [8], [20], [21], and [29]. Also, an RC for  $LCL$ -filtered grid-following converters was proposed in [36]. Inspired by these studies, this work has developed a high-performance RC implemented in the discrete-time domain for voltage regulation of GFCs, which is capable of regulating the unbalanced/nonlinear loads and avoiding the constraints faced by the existing RCs.

The rest of this article is organized as follows. Section II begins by modeling the  $LC$ -filtered GFCs in the discrete-time domain. Optimal tuning of the current controller through active damping optimization is

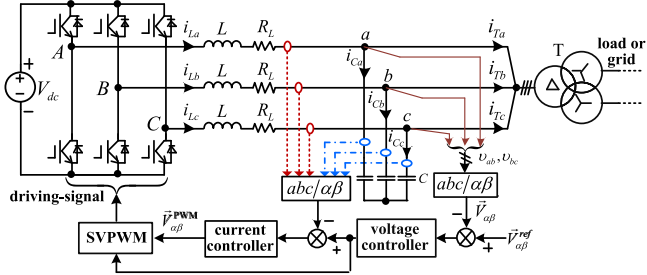


Fig. 1. Three-phase  $LC$ -filtered GFCs with the dual-loop voltage–current control scheme.

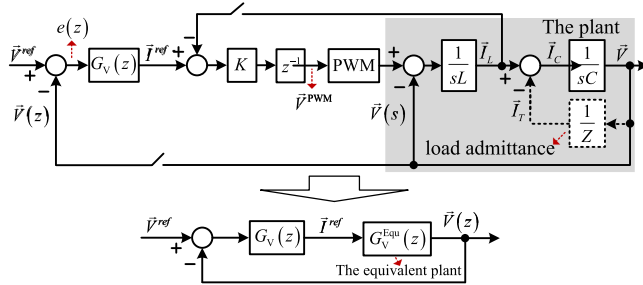


Fig. 2. Dual-loop voltage–current control method for GFCs.

presented in Section III, where the original plant, the one-sampling delay, and the current gain are considered as the equivalent plant of the voltage controller. The effectiveness of PR and VPI for voltage regulation of GFCs is analyzed more deeply in Section IV to better identify their features and constraints. The proposed RC for voltage regulation of GFCs is also addressed in this section. Effectiveness of the developed controller is verified through experiments in Section V. Finally, Section VI concludes this article.

## II. SYSTEM MODELING IN THE DISCRETE-TIME DOMAIN

Fig. 1 shows a three-phase GFCs with an output  $LC$  filter, where  $L$  is the filter inductor and  $C$  is the filter capacitor. If necessary, a transformer  $T$  can be employed at the output of the converter, which is commonly required for applications with a four-wire structure and/or where isolation is required. It should be noted that  $R_L$  is the series equivalent resistance, which is employed for emulating the power losses of the converter (mainly from the inductors and power switches). It should be noted that in this work, the capital letter hatted with  $\rightarrow$  represents the electrical vector, for instance,  $\vec{V} = v_\alpha + jv_\beta$  represents the output voltage vector, which can also be applied to other electrical variables. Also shown in this figure is the dual-loop voltage–current control method. It should be noted that either the inductor current  $i_L$  or the capacitor current  $i_C$  can be sensed and fed back for regulation, as shown in Fig. 1. In this article, the inductor current  $i_L$  is measured since it can be employed for overcurrent protection of the converter.

To illustrate, the dual-loop control scheme is further plotted in Fig. 2, where  $G_V(z)$  is the voltage controller and  $K$  is the current controller, which is a proportional gain, as discussed in [8], [18], [19], and [22]. It can be noted that the continuous  $LC$  filter has

been noted in the  $s$ -domain (the shaded part), and the digital controller and modulation have been noted in the  $z$ -domain. In the following study of this work, the equivalent resistance  $R_L$  is ignored, i.e.,  $R_L = 0$  in Fig. 2, in order to emulate the worst case without any physical damping for the filter.

To begin with, the following equation can be deduced from the observation of Fig. 2:

$$\begin{cases} \left[ \vec{V}^{\text{PWM}}(s) - \vec{V}(s) \right] \cdot \frac{1}{s \cdot L} = \vec{I}_L(s) \\ \left[ \vec{I}_L(s) - \vec{I}_T(s) \right] \cdot \frac{1}{s \cdot C} = \vec{V}(s) \end{cases}. \quad (1)$$

Conceptually, as shown in (1), with regard to  $\vec{V}$ , the load current  $\vec{I}_T$  features a disturbance characteristic, whose effects can be reduced by sensing the load current and employing a feedforward method in Fig. 2, as addressed in [22]. An additional sensor for measuring  $\vec{I}_T$  is, however, required for this method. Nevertheless, in the steady state, the voltage caused by  $\vec{I}_T$  can be ignored, since  $G_V(z)$  can be designed to have infinite open-loop gains at both the positive sequence (PS) and the NS of the selected frequencies.

Transfer functions for relating the controller output voltage  $\vec{V}^{\text{PWM}}$  to the capacitor voltage  $\vec{V}$  and the inductor current  $\vec{I}_L$  can, therefore, be derived from (1), which can be expressed as follows:

$$G_V^{\text{PL}}(s) = \frac{\vec{V}(s)}{\vec{V}^{\text{PWM}}(s)} = \frac{1}{s^2 LC + 1} = \frac{\omega_{\text{res}}^2}{s^2 + \omega_{\text{res}}^2} \quad (2)$$

$$G_{iL}^{\text{PL}}(s) = \frac{\vec{I}_L(s)}{\vec{V}^{\text{PWM}}(s)} = \frac{s \cdot C}{s^2 LC + 1} = \frac{1}{L} \cdot \frac{s}{s^2 + \omega_{\text{res}}^2} \quad (3)$$

where  $\omega_{\text{res}} = \sqrt{1/L \cdot C}$  is the filter resonance frequency.

Expressions (2) and (3) can next be transformed to the  $z$ -domain by applying the zero-order holder discretization, since the controller output voltage  $\vec{V}^{\text{PWM}}$  is calculated and kept constant during each sampling interval. The resulting transfer functions can be expressed as follows:

$$G_V^{\text{PL}}(z) = \frac{(z+1) \cdot (1 - \cos(\omega_{\text{res}} \cdot T_s))}{z^2 - 2z \cdot \cos(\omega_{\text{res}} \cdot T_s) + 1} \quad (4)$$

$$G_{iL}^{\text{PL}}(z) = \frac{1}{\omega_{\text{res}} \cdot L} \cdot \frac{\sin(\omega_{\text{res}} \cdot T_s) \cdot (z-1)}{z^2 - 2z \cdot \cos(\omega_{\text{res}} \cdot T_s) + 1} \quad (5)$$

where  $T_s$  is the sampling period.

## III. TUNING OF THE CURRENT CONTROLLER BASED ON ACTIVE DAMPING OPTIMIZATION

Focusing on the objective of active damping for the resonance of the filter, this section proposes a tuning method for the current controller  $K$  based on the discrete root locus analysis to achieve the possible maximum active damping. To begin with, by combining (4) and (5), the equivalent plant with regard to the voltage controller  $G_V(z)$ , noting as  $G_V^{\text{Equ}}(z)$  in Fig. 2, can be derived as follows:

$$G_V^{\text{Equ}}(z) = \frac{K \cdot [1 - \cos(\omega_{\text{res}} T_s)] \cdot (z+1)}{z^3 - 2z^2 \cos(\omega_{\text{res}} T_s) + (1+a)z - a} \quad (6)$$

where  $a = K \cdot \sin(\omega_{\text{res}} T_s) / (\omega_{\text{res}} L)$ .

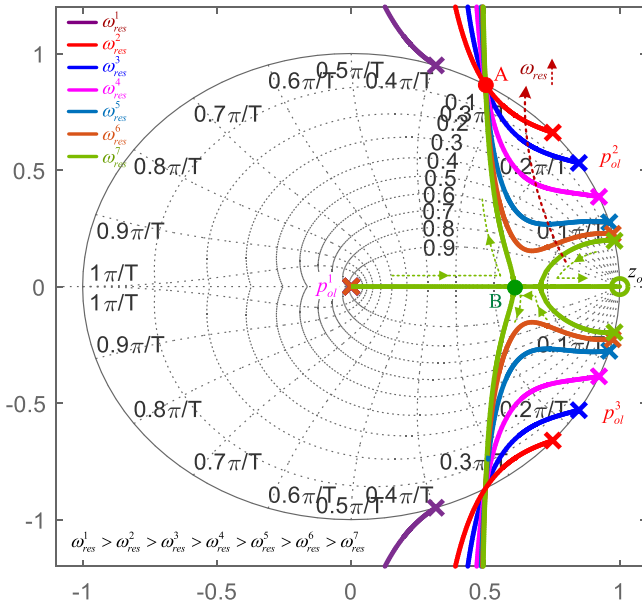


Fig. 3. Root locus of  $G_V^{\text{Equ}}(z)$  with the variation of  $K$  for different  $\omega_{\text{res}}$ .

By varying  $K$  from 0 to  $+\infty$ , the root locus of (6) for different resonant frequencies  $\omega_{\text{res}}$  can be depicted in Fig. 3. Specifically,  $L = 0.4 \text{ mH}$ , and the capacitor is 30, 80, 150, 300, 500, 800, and  $1000 \mu\text{F}$  for  $\omega_{\text{res}}^{1,2,3,4,5,6,7}$ , respectively. Some observations noted can be expressed as follows.

- For the evaluated cases of  $\omega_{\text{res}}^{1,2,3,4,5,6,7}$ , the poles of  $p_{ol}^{2,3}$  related to the filter resonance are moving inside of the unit circle, and accordingly, the active damping of these poles is increasing.
- As  $K$  continues to increase, the poles of  $p_{ol}^{2,3}$  turn to move toward the unit circle, and the cures of different  $\omega_{\text{res}}$  cross the unit circle at the same point, noting A in Fig. 3. However, for  $\omega_{\text{res}}$  higher than the frequency related to the common crossover point, the plant cannot be damped by this method, which is the case of  $\omega_{\text{res}}^1$  shown in Fig. 3, where  $p_{ol}^{2,3}$  are always lying outside of the unit circle regardless of the value of  $K$ . This can be avoided by reducing the cutoff frequency of the filter and/or increasing the sampling frequency  $f_s = 1/T_s$ .
- Typically, for the case of  $\omega_{\text{res}}^7$ , a unity value of active damping can be expected since all the poles can be set on the real axis simultaneously. This characteristic is the same as that addressed in [19], where unity value of damping is preferred.
- It should be emphasized that the equivalent plant features the nonminimum phase system characteristic if the poles lie outside of the unit circle, which is certainly undesired and should be avoided.

For clear illustration, for the poles of  $p_{ol}^{1,2,3}$ , the active damping  $\xi$  with respect to  $K$ , which is shown in Fig. 4, can be derived based on (23). First, regarding  $\omega_{\text{res}}^{2,3,4,5,6}$ , as shown in Fig. 4(a),  $\xi$  for  $p_{ol}^{2,3}$  reaches its peak value for a certain value of  $K$ . For instance, for  $\omega_{\text{res}}^3$ ,  $\xi_{\max} = 0.19$  for  $K = 1.12$ . It should be emphasized that the minimization of the distance between the

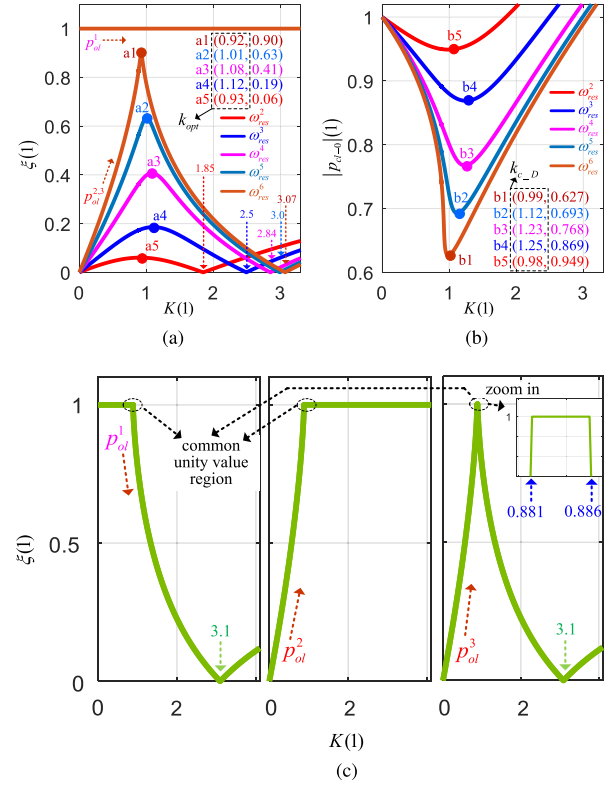


Fig. 4. (a)  $K$  versus active damping  $\xi$  of  $p_{ol}^{1,2,3}$  for  $\omega_{\text{res}}^{2,3,4,5,6}$ , (b)  $K$  versus  $|p_{cl,0}|$  of  $p_{ol}^{2,3}$  for  $\omega_{\text{res}}^{2,3,4,5,6}$ , and (c)  $K$  versus active damping  $\xi$  of  $p_{ol}^{1,2,3}$  for the case of  $\omega_{\text{res}}^7$ .

dominant poles  $p_{cl}^{2,3}$  and the original point, i.e.,  $|p_{cl,0}|$ , is not equivalent to the maximization of the active damping, as shown in Fig. 4(a) and (b), in which  $k_{\text{opt}} \neq k_{c,D}$  for  $\omega_{\text{res}}^{2,3,4,5,6}$  can be noted. Nevertheless, this parabolic shape depicted in Fig. 4(a) is slightly different for the case of  $\omega_{\text{res}}^7$ , whose  $\xi$  versus  $K$  is shown in Fig. 4(c). The difference lies in that the points of  $K \rightarrow \infty$  for the curves initiating from  $p_{ol}^{1,2}$  have exchanged compared to that of  $\omega_{\text{res}}^{2,3,4,5,6}$ . Nevertheless,  $\xi$  for the curve starting from  $p_{ol}^3$  remains the same and reaches its unity value for  $0.881 \leq K \leq 0.886$ , which is also the common unity value region of  $\xi$  for the poles starting from  $p_{ol}^{1,2}$ .

To sum up, the optimum value of  $K$  can be determined to obtain the peak value of  $\xi$  for  $\omega_{\text{res}}^{2,3,4,5,6}$  from Fig. 4(a). On the other hand, for the case of  $\omega_{\text{res}}^7$ , a higher value of  $K$  to get the unity damping is preferred since the damped poles are more inside the unit circle, i.e., higher value of magnitude (see point B in Fig. 3). Hence,  $K = 0.886$  is selected for  $\omega_{\text{res}}^7$ . From the above analysis, it can be noted that a higher value of  $\xi$  can be obtained for a reduced  $\omega_{\text{res}}$ . This is, however, not preferred, and the reason can be explained as follows: 1) a reduced  $\omega_{\text{res}}$  commonly results in a large value of the filter capacitor, which is bulky and can lead to increased no-load current and reduced efficiency and 2) also, reduced  $\omega_{\text{res}}$  can bring in highly increased impedance, especially for high-order currents. Therefore, the capacity of the converter can be greatly constrained in order to avoid overmodulation, since the voltage  $V^{\text{PWM}}$  has compensated the voltage droop across the filter.

TABLE I  
PARAMETERS OF THE SETUP

Switch frequency	$f_{sw}$	4kHz
Sampling frequency	$f_s = 2f_{sw}$	8kHz
Inductance	$L$	0.4mH
Capacitor	$C$ for $\omega_{res}^3$	150 $\mu$ F
Capacitor	$C$ for $\omega_{res}^5$	500 $\mu$ F
Capacitor	$C$ for $\omega_{res}^7$	1000 $\mu$ F
balanced/unbalanced resistive load	$R_{load}$	$\approx 2.6\Omega$
diode rectifier load	$R_{rec}$	$\approx 4.2\Omega$
three-phase inductive load	reactive power	65kVar

With the above method, the explicit optimum gain for  $K$  can be obtained to achieve the possible maximum active damping, which is the basis for the analysis and design of the outer voltage controller, as addressed in the following sections.

#### IV. HIGH-PERFORMANCE DISCRETE RESONANT CONTROLLER FOR VOLTAGE REGULATION OF GFCs

In this section, the effectiveness and constraints faced by both PR and VPI for voltage regulation of GFCs have been identified. Then, the developed high-performance discrete resonant controller (dRC) consisting of the PS and NS complex-coefficient vector controller is addressed.

##### A. Analysis of the Effectiveness of PR and VPI for Voltage Regulation of GFCs

The cases of  $\omega_{res}^{3,5,7}$  in Fig. 3 are employed for the subsequent analysis, whose parameters are shown in Table I. Hence,  $K = 1.12, 1.01$ , and  $0.886$  can be appreciated for the considered three cases from the above analysis, as shown in Fig. 4. It should be mentioned that the detailed transfer function for PR and VPI, noting as  $G_{PR}(z)$  in (7) and  $G_{VPI}(z)$  in (8), respectively, can be obtained with the prewrapped Tustin discretization to the continuous-time transfer function, as approached in [37]. The detailed expressions of (7) and (8) have been well established in the existing studies and, hence, will not be elaborated in this article

$$G_{PR}^d(z) = K_p + \sum_{h=1}^N K_i^h R_{tp}^{1d}(z) \quad (7)$$

$$G_{VPI}^d(z) = \sum_{h=1}^N K^h [R_{tp}^{1d}(z) + R_{tp}^{2d}(z)] \quad (8)$$

where  $N$  is the number of parallel resonant terms. The tuning and delay compensation method developed in [29] for RCs is employed here. In case PR is employed for voltage regulation, the closed-loop frequency response is depicted in Fig. 5(a) and (d). Some observations noted can be described as follows.

- As shown in Fig. 5(a), where  $K_p = 0.07$  and  $K_i^h = 1$  are employed, it can be observed that there is a weekly damped region even with the optimum active damping  $K$  employed. This phenomenon is related to the equivalent

plant  $G_V^{Equ}$  whose weekly damped poles can be noted from Fig. 3.

- Although the system is stable and no anomalous peaks have been found, this is, however, achieved at the cost of limited bandwidth at the selected frequencies, resulting in a slow transient response of the output voltage. To increase the bandwidth, the case of  $K_i^1 = 25$  and  $K_i^h = 5$  for  $h \neq 1$  is evaluated. As shown in Fig. 5(d), closed-loop anomalous peaks appear as noted in the red circle. This should be avoided since it can cause fluctuation in the output voltage. If  $K_p = 0$  in (7), i.e., only the resonant term is employed as the case addressed in [24], the above conclusion drawn from  $K_p \neq 0$  can still be valid, as shown in Fig. 5(b) and (e), where both the weekly damped region and anomalous peaks can be observed.
- Also, for the case of the employment of VPI for  $G_V(z)$ , the same conclusion as that of PR can be reached from Fig. 5(a) and (f). Specifically, by comparing Fig. 5(a)–(c) and Fig. 5(d)–(f), it can be observed that these frequency responses are very similar, which means that the advantages of VPI compared to that of PR, as addressed in [29], [30], and [37], are no longer valid in this case.
- For low values of  $\omega_{res}$ , as shown in Fig. 6 for  $\omega_{res}^5$ , the weekly damped region, which is relatively flattened compared to that of  $\omega_{res}^3$ , now moves toward lower frequencies. Alternatively, for the case of  $\omega_{res}^7$  whose active damping can be unity, the weekly damped region is much flattened and broadened. In this manner, the bandwidth around the resonant terms of lower frequencies has been much improved, for the employment of either PR or VPI, as shown in Fig. 7(a) and (b), respectively. This is, however, at the cost of bulky-sized filter and constrained capacity of the converter for high-frequency load currents, as addressed earlier.
- By the way, increasing the sampling frequency has the similar effect as that of reducing  $\omega_{res}$ , and hence, this aspect will not be further elaborated here. Nonetheless, increasing the switching frequency (the sampling frequency is commonly the same as or twice of the switching frequency) may not be available for high-power applications, which commonly feature a low switching frequency characteristic to reduce the power loss.
- To sum up, for a reasonably designed GFCs, especially the high-power applications, the equivalent plant commonly features a week damping characteristic; tuning of the voltage loop has to make a compromise between the terms of stability, anomalous peaks avoidance, and loop bandwidth for both PR and VPI controllers. It should be emphasized that the existence of the weekly damped region cannot be avoided through tuning of the controller's gain in (7) and (8).

##### B. Development of the Discrete Complex-Coefficient Voltage Controller in the PS-SRF

First, the expression of the equivalent plant in the PS-SRF can be obtained with the replacement of  $z$  with  $(z \cdot e^{j \cdot \omega_e \cdot T_s})$  in (6),

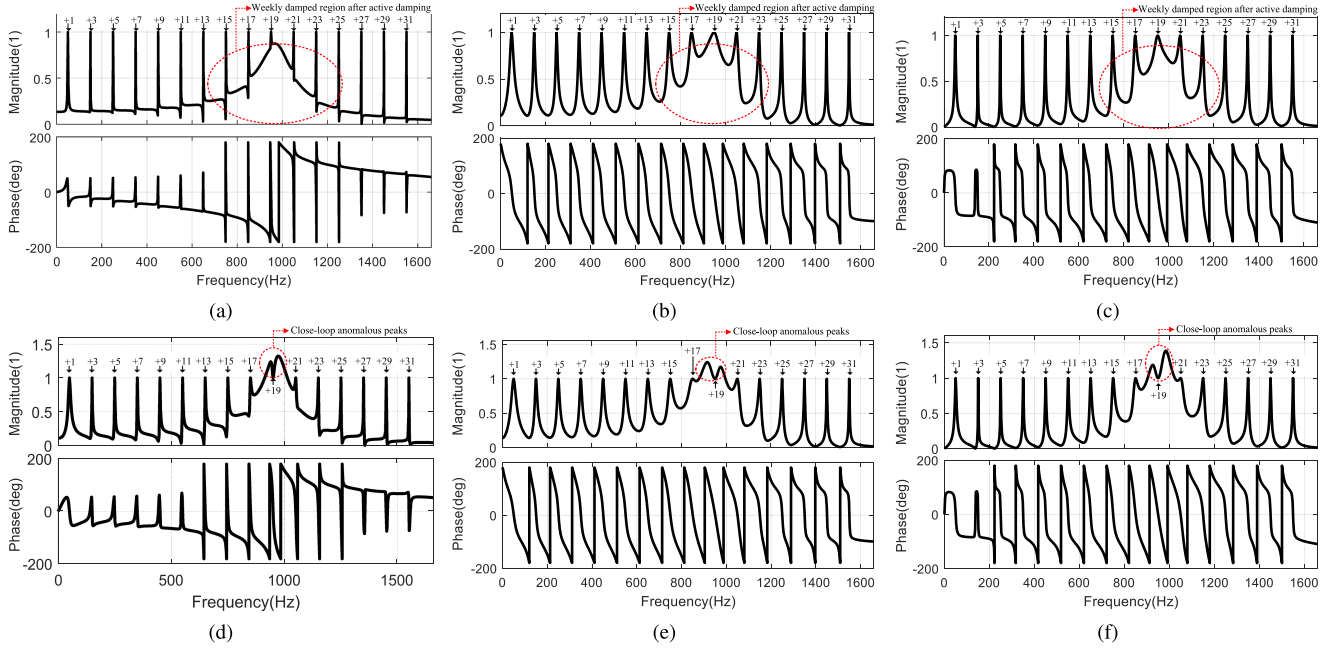


Fig. 5. Closed-loop frequency response of the voltage loop for the case of  $\omega_{\text{res}}^3$ , where (a) PR is employed with  $K_p = 0.07$  and  $K_i^h = 1$ , (b) PR is employed with  $K_p = 0$  and  $K_i^h = 10$ , (c) VPI is employed with  $K^1 = 36$  and  $K^h = 2.4$  for  $h \neq 1$ , (d) PR is employed with  $K_p = 0.07$ ,  $K_i^1 = 25$ , and  $K_i^h = 5$  for  $h \neq 1$ , (e) PR is employed with  $K_p = 0$ ,  $K_i^1 = 40$ , and  $K_i^h = 15$  for  $h \neq 1$ , and (f) VPI is employed with  $K^1 = 48$  and  $K^h = 3.2$  for  $h \neq 1$ .

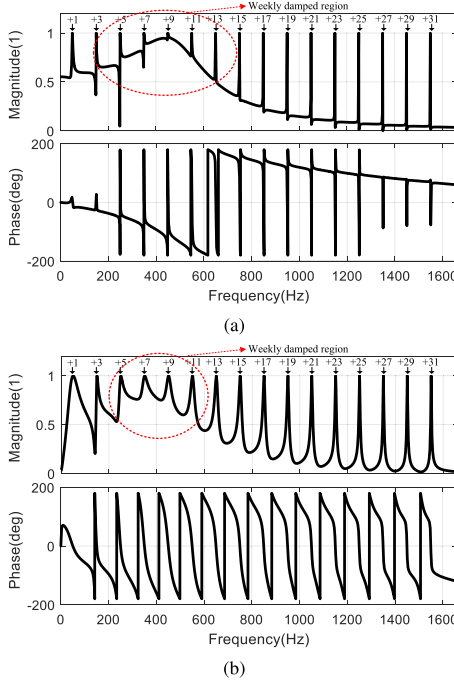


Fig. 6. Closed-loop frequency response of the voltage loop for the case of  $\omega_{\text{res}}^5$ , where (a) PR is employed with  $K_p = 0.06$ ,  $K_i^1 = 3$ , and  $K_i^h = 1$  for  $h \neq 1$  and (b) VPI is employed with  $K^1 = 48$  and  $K^h = 3.2$  for  $h \neq 1$ .

which can be expressed as follows:

$$G_V^{\text{Equ-PS-SRF}}(z) = \frac{K \cdot [1 - \cos(\omega_{\text{res}} \cdot T_s)] \cdot (ze^{j \cdot \omega_e \cdot T_s} + 1)}{z^3 \cdot e^{j3\omega_e \cdot T_s} - z^2 \cdot b + (1+a)ze^{j \cdot \omega_e \cdot T_s} - a} \quad (9)$$

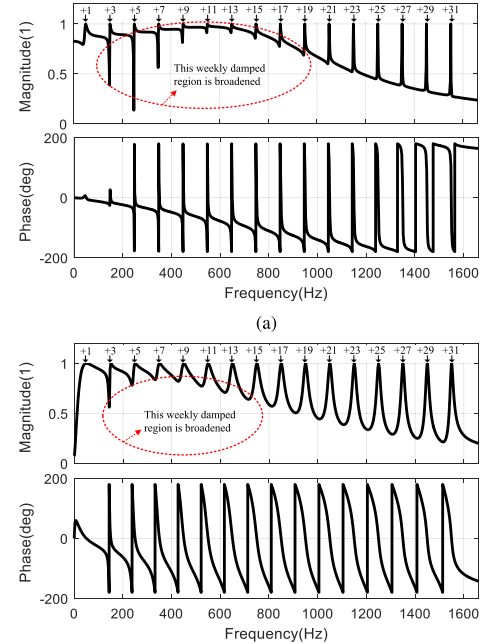


Fig. 7. Closed-loop frequency response of the voltage loop for the case of  $\omega_{\text{res}}^7$ , where (a) PR is employed with  $K_p = 0.12$ ,  $K_i^1 = 3$ , and  $K_i^h = 1$  for  $h \neq 1$  and (b) VPI is employed with  $K^1 = 60$  and  $K^h = 4.5$  for  $h \neq 1$ .

where  $b = 2 \cdot e^{j2 \cdot \omega_e \cdot T_s} \cdot \cos(\omega_{\text{res}} \cdot T_s)$ ,  $\omega_e$  is the fundamental frequency of the output voltage, and  $a = K \cdot \sin(\omega_{\text{res}} T_s) / (\omega_{\text{res}} L)$  is the same as that in (6).

The weekly damped poles of (9) can be canceled by the matching zeros provided by the developed controller, in order to avoid the adverse effects, as addressed before. Another requirement for the controller is that the order of the denominator has to be equal to or higher than that of the numerator, in order to make the controller be realizable practically. The developed discrete complex-coefficient voltage controller is expressed as follows:

$$G_V^{\text{PS-SRF}}(z) = k_V \cdot \frac{z^3 e^{j3\omega_e T_s} - z^2 \cdot b + (1+a) z e^{j\omega_e T_s} - a}{z \cdot (z-1) \cdot (z e^{j\omega_e T_s} + 1)} \quad (10)$$

where  $k_V$  is the gain of the controller, and  $b = 2 \cdot e^{j2\omega_e T_s} \cos(\omega_{\text{res}} \cdot T_s)$  is the same as the one in (9). It can be noted that the term  $(z-1)$  has infinite gain for the dc signal, which guarantees zero steady-state tracking error for the dc component in the PS-SRF. In this manner, regulation of the PS voltage with zero steady-state error is achieved in the stationary reference frame equivalently.

The open-loop transfer function of voltage loop can be obtained by replacing  $G_V(z)$  with  $G_V^{\text{PS-SRF}}(z)$  and  $G_V^{\text{Equ}}(z)$  with  $G_V^{\text{Equ-PS-SRF}}(z)$  in Fig. 2, which is shown as follows:

$$G_{\text{OL}}^{\text{PS-SRF}}(z) = k_V \cdot \frac{K \cdot [1 - \cos(\omega_{\text{res}} \cdot T_s)]}{z \cdot (z-1)}. \quad (11)$$

Performance evaluation of the controller can be performed based on (11). Here,  $\omega_{\text{res}}^3$  is employed for analysis, which is also the case of the setup. As shown in Fig. 8(a), the root locus is plotted by varying the controller gain  $k_V$  from 0 to  $+\infty$ . It should be mentioned that the damping and magnitude of the poles, instead of the distance between the poles and the original point as addressed in [24], are employed for investigation in this work, since the transient response of a particular pole can, theoretically, be characterized by its own damping and magnitude. It should be noted that the transient response can be different for poles with a common distance to the original point in the  $z$ -plane, since either the damping or the magnitude can vary dramatically. To be specific, the magnitude and damping of the poles  $p_{cl}^{1,2}$  can be calculated with (20) and (23), respectively, resulting the plots of  $k_V$  versus  $\xi$  and  $k_V$  versus  $|p_{cl}(z)|$  shown in Fig. 8(b) and (c), respectively. Some observations noted can be summarized as follows.

- 1) For small values of  $k_V$ , i.e.,  $k_V < 0.6$ , the system features an overdamping characteristic since  $\xi = 1$  is valid for  $p_{cl}^{1,2}$  in this case.
- 2) For  $k_V > 0.6$ , as shown in Fig. 8(b),  $\xi$  for  $p_{cl}^{1,2}$  decreases sharply. Therefore, the system has an underdamping characteristic for  $k_V \in (0.6, 2.42)$ .
- 3) Typically, for  $k_V = 2.42$ , the system is critically damped. This characteristic is very similar to the conclusions addressed in [29] and [30], where the tuning of the cPI controller for current regulation grid-following converter based on the optimization of overshoot and settling time is investigated.

Also, performance evaluation of (11) in terms of parameter variation of the filter is performed, since the inductance of  $L$  can vary with the temperature and the current flowing through it.

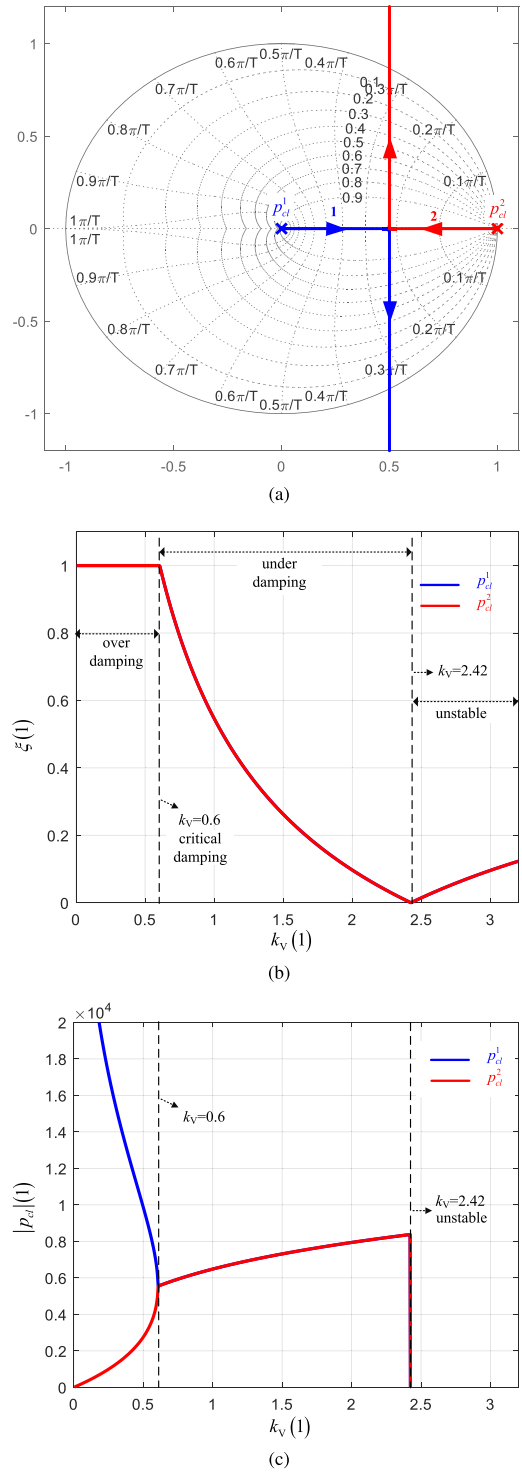


Fig. 8. (a) Root locus of the voltage loop with the employment of  $G_V^{\text{PS-SRF}}(z)$ . (b) Plot of  $k_V$  versus  $\xi$ . (c) Plot of  $k_V$  versus  $|p_{cl}(z)|$ .

According to the datasheet of the inductor employed in the setup, the inductance of  $L$  at rated current is reduced to approximately 75% of its designed value  $L_{\text{rel}}$ . Hence, the maximum detuning of  $L = 0.7L_{\text{rel}}$  is employed for the subsequent analysis. As shown in Fig. 9(a), for the considered cases of  $L = 0.9L_{\text{rel}}$ ,  $L = 0.8L_{\text{rel}}$ , and  $L = 0.7L_{\text{rel}}$ , it can be observed that filter parameter detuning has negligible influence on the frequency response around  $\omega_e$ .

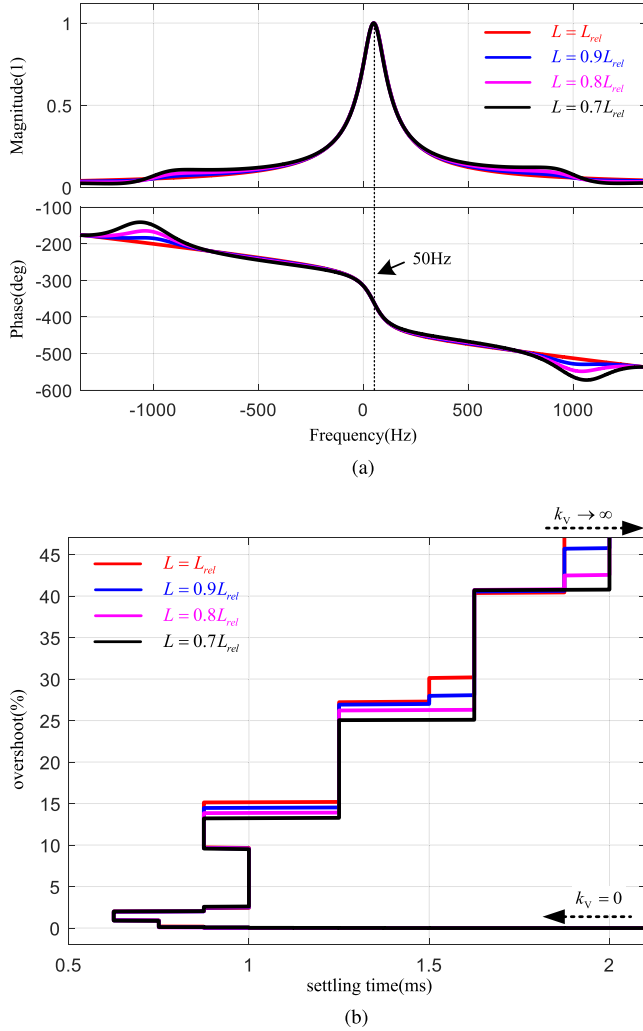


Fig. 9. Evaluation of parameter detuning for  $L \neq L_{\text{rel}}$ , where (a) is closed-loop frequency response and (b) is the plot of settling time versus overshoot of the step response for a sweep of  $k_V = 0 \rightarrow \infty$ .

Also, the difference at higher frequencies can cause limited difference since the magnitude is highly reduced. This can also be appreciated from the plot of settling time versus overshoot shown in Fig. 9(b), which is obtained from the step response for a sweep of  $k_V = 0 \rightarrow \infty$ .

Since cPI can further lead to the high-performance RC, i.e., VPI (for current regulation of grid-following converters), an RC (for voltage regulation of GFCs) whose performance is similar to that of VPI can be expected based on the developed controller of (10), which will be addressed in the subsequent part of this section.

### C. High-Performance dRC for Voltage Regulation of GFCs

Following the above procedure, the discrete complex coefficient voltage controller for the NS voltage regulation can be developed in the NS-SRF, whose transfer function is

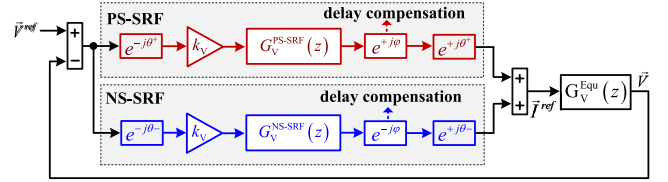


Fig. 10. Dual SRF control based on the developed PS- and NS-SRF complex-coefficient voltage controller.

expressed as follows:

$$G_V^{\text{NS-SRF}}(z) = k_V \cdot \frac{z^3 e^{-j3\omega_e \cdot T_s} - z^2 \cdot c + (1+a)ze^{-j\omega_e \cdot T_s} - a}{z \cdot (z-1)(ze^{-j\omega_e \cdot T_s} + 1)} \quad (12)$$

where  $c = 2 \cdot e^{-j2\omega_e \cdot T_s} \cdot \cos(\omega_{\text{res}} \cdot T_s)$ . Based on the dual-SRF control method [38], [39],  $G_V^{\text{PS-SRF}}(z)$  of (10) and  $G_V^{\text{NS-SRF}}(z)$  of (12) can be employed for the regulation of PS and NS voltages simultaneously with zero steady-state error, as shown in Fig. 10. It should be noted that the terms of  $e^{+j\varphi}$  and  $e^{-j\varphi}$  are included for delay compensation, which is a rule of thumb for RCs to improve the system's stability, such as PR and VPI addressed in [29].

The dRC implemented in the stationary reference frame can be finally derived from Fig. 10, which is expressed as follows:

$$\begin{aligned} G_V^{\text{dRC}}(z) &= G_V^{\text{PS-SRF}}(z \cdot e^{-j\omega_e \cdot T_s}) \cdot e^{+j\varphi} \\ &\quad + G_V^{\text{NS-SRF}}(z \cdot e^{+j\omega_e \cdot T_s}) \cdot e^{-j\varphi} \\ &= K_V \frac{a_0 + a_1 z^{-1} + a_2 z^{-2} + a_3 z^{-3} + a_4 z^{-4}}{1 + b_1 \cdot z^{-1} + b_2 \cdot z^{-2} + z^{-3}} \\ &= K_V \cdot R_d(z) \end{aligned} \quad (13)$$

where  $K_V = 2k_V$ , and expressions for the coefficients are given as follows:

$$b_1 = b_2 = 1 - 2 \cos(\omega_e \cdot T_s)$$

$$a_0 = \cos(2\omega_e \cdot T_s + \varphi)$$

$$a_1 = -2 \cos(2\omega_e T_s + \varphi) \cos(\omega_{\text{res}} T_s) - \cos(\omega_e T_s + \varphi)$$

$$a_2 = (1+a) \cos(2\omega_e T_s + \varphi) + 2 \cos(\omega_{\text{res}} T_s) \cos(\omega_e T_s + \varphi)$$

$$a_3 = -a [\cos(2\omega_e T_s + \varphi) + \cos(\omega_e T_s + \varphi)] - \cos(\omega_e T_s + \varphi)$$

$$a_4 = a \cdot \cos(\omega_e \cdot T_s + \varphi). \quad (14)$$

Again,  $a = K \cdot \sin(\omega_{\text{res}} T_s) / (\omega_{\text{res}} L)$  is the same as the one in (6) and (9). It can be noted from (14) that all the parameters are determined except  $\varphi$ . It should be mentioned that for GFCs, the excitation frequency  $\omega_e$  is also a known variable, which can be determined from the droop/VSG block, the secondary frequency restoration block. It has been proved that  $\varphi$  is closely related to the position of the asymptotic line of the Nyquist diagram at the frequency  $\omega_e$ , which in Fig. 11 is noted as  $\gamma$ . However, it is very difficult to derive the exact expression of  $\gamma$  through  $G_V^{\text{dRC}}(z)$  and  $G_V^{\text{Equ}}(z)$ , since their expressions are extremely complicated.

This can be avoided through the employment of  $G_V^{\text{PS-SRF}}(z)$  in (10) and  $G_V^{\text{Equ-PS-SRF}}(z)$  in (9), since the value of  $\varphi$  is

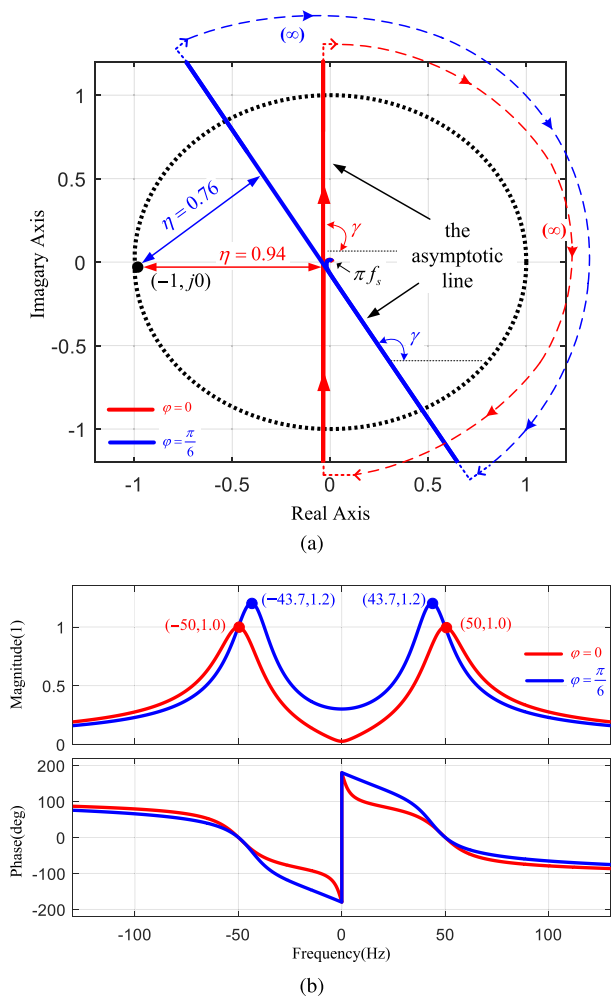


Fig. 11. (a) Nyquist diagram of the voltage loop for  $\omega_e = 100\pi$ . (b) Closed-loop frequency response of the voltage loop for different values of  $\varphi$ .

the same for the PS-SRF and NS-SRF controller, as shown in Fig. 10. Thanks to the pole/zero cancellation characteristic of (9) and (10), the open-loop transfer function in the stationary reference frame can be derived easily, which is expressed as follows:

$$G_{V\_OL}^{PS}(z) = k_V \frac{K \cdot [1 - \cos(\omega_{res} \cdot T_s)]}{z \cdot e^{-j\omega_e T_s} \cdot (z \cdot e^{-j\omega_e T_s} - 1)} \cdot e^{j\varphi}. \quad (15)$$

Since  $k_V \cdot K \cdot [1 - \cos(\omega_{res} \cdot T_s)] > 0$  is always valid, the phase of the numerator of (15) at the frequency  $\omega_e$  is  $\varphi$ . The denominator is also 0 if  $z = e^{j\omega_e T_s}$  is substituted to (15), but, in fact, the phase of the denominator at  $\omega_e$  is not 0. This is because for  $\omega \rightarrow \omega_e^-$ , the term  $z \cdot e^{-j\omega_e T_s}$  becomes  $e^{j(\omega - \omega_e)T_s}$ , whose phase is  $-\pi/2$  since  $\omega < \omega_e$ . Also,  $\angle(z \cdot e^{-j\omega_e T_s} - 1) = 0$  can be appreciated with the same method. Therefore, the phase of the asymptotic line of the Nyquist diagram at the frequency  $\omega_e$  can be derived as follows:

$$\gamma = \frac{\pi}{2} + \varphi. \quad (16)$$

It has been proved that the increase in  $\varphi$  will lead to the decrease in the minimum distance of the Nyquist diagram to the critical point  $(-1, j0)$ , which can be observed from Fig. 11(a),

where  $\eta$  is reduced to 0.76 for the case of  $\varphi = \pi/6$  from 0.94 for  $\varphi = 0$ . Also, the most enhanced stability and avoidance of anomalous peak can be achieved when the asymptotic line crosses the real axis vertically [29], i.e.,  $\varphi = \pi/2$ , which, combining with (16), yields

$$\varphi = 0. \quad (17)$$

Also, the closed-loop frequency response of  $\omega_e = 100\pi$  for different  $\varphi$  is illustrated in Fig. 11(b), where it can be noted that zero steady-state tracking error has been achieved for both the PS and NS signals, and the anomalous peaks resulted from  $\varphi = \pi/6$  are avoided after the delay compensation of (17) is employed. Also, it should be emphasized that the magnitude of the closed-loop frequency response for the dc signal is very limited (almost zero) with employment of the delay compensation (17), unless an exceptionally large value of  $K_V$  is employed. In other words, the proposed controller  $G_V^{dRC}(z)$  has major contribution to dc-signal suppression, which can be resulted from sensors, analog signal conditioning circuits, and/or operational amplifiers. This is good news for the transformer, which may be connected at the output terminal of GFCs, since the dc voltage can cause severe saturation and failure to the transformer.

High-frequency resonant terms can next be included by replacing  $\omega_e$  with  $h\omega_e$  in (13), resulting in the controller  $\sum_{h=1}^N K_V^h \cdot R_d^h(z)$ . In this manner, the asymptotic lines at the selected frequencies cross the real axis vertically, as shown in Fig. 12(a) and (b). The method proposed in [29] can also be employed for tuning of the controller gain  $K_V^h$  here. The key is to keep  $\eta \geq 0.5$  in the Nyquist diagram. In this work, the gain for the fundamental voltage resonant term is tuned to be relative larger than that for the high-frequency resonant terms. In this manner, a higher bandwidth at the fundamental frequency is achieved, as shown in Fig. 12(c), resulting in a fast response since the output voltage mainly consists of the fundamental component. Specifically,  $K_V^1 = 0.5$  and  $K_V^h = 0.02$  for  $h \neq 1$  are employed.

Also, by comparing Figs. 5 and 12(c), it can be observed that the developed dRC controller has solved the issues of the weekly damped region and the constrained bandwidth faced by the existing RCs (both PR and VPI).

## V. EXPERIMENTAL RESULTS

The experimental setup is shown in Fig. 13, where it can be noted that it consists of input and output transformers, a diode rectifier, and an inverter. The rated power of the setup is 500 kW. The input transformer, whose input and output voltages are 10 kV and 500 V, respectively. The diode rectifier, the inverter, and the digital controller are depicted in Fig. 13(b). The digital controller is mainly made of a DSP (TMS320C28346), a field-programmable gate array (FPGA) (EP3C16), and other auxiliary circuits for signal conditioning, analog-to-digital conversion, and communication. Measuring equipment include a ScopeCorder, a PW3198 power quality analyzer, three differential probes, and three current probes. Parameters of the setup are the same as those shown in Table I. The signal sampling is performed at both peaks and valleys of the triangular carrier signal, which means that the sampling frequency is twice of

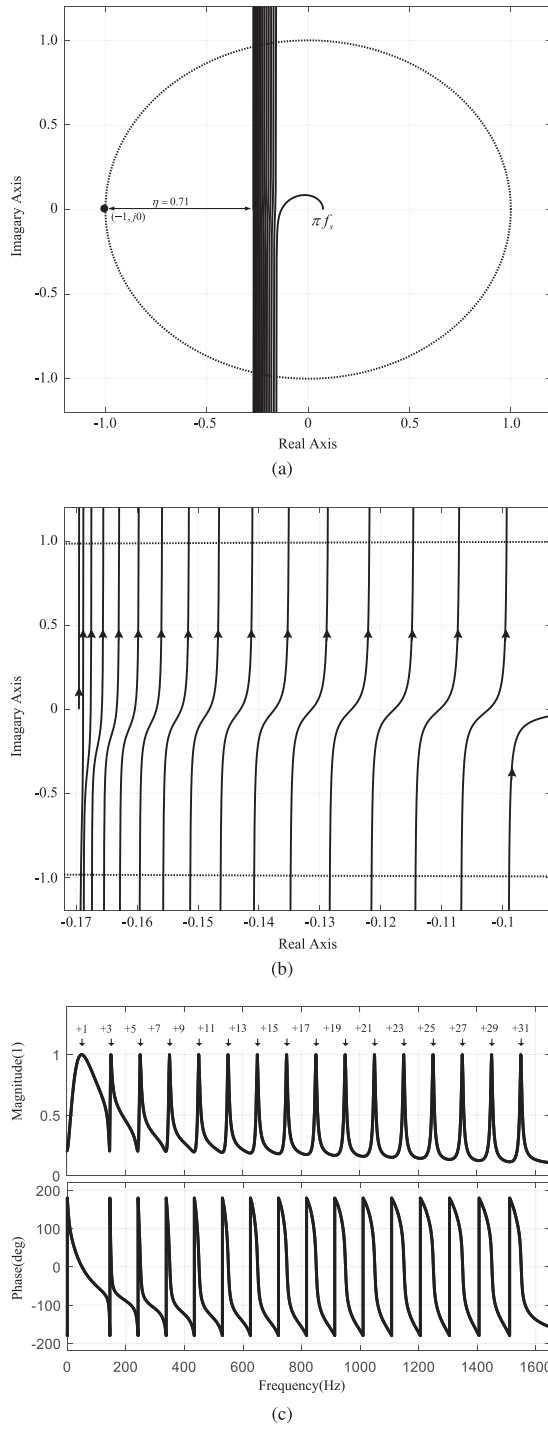


Fig. 12. (a) Nyquist diagram of the voltage loop with the employment of the developed  $G_V^{dRC}$  controller for  $h$  up to 31. (b) Zoomed-in part of (a) around the asymptotic lines. (c) Closed-loop frequency response of the voltage loop.

the switching frequency, as shown in Table I. In particular, the ScopeCorder is set as follows: 1)  $v_{ab}$ ,  $v_{bc}$ , and  $v_{ca}$  with 300 V/div and 2)  $i_a$ ,  $i_b$ , and  $i_c$  with 100 A/div. As shown in Fig. 13(a), three types of typical loads, including three-phase balanced, unbalanced, and nonlinear loads, whose parameters are shown in Table I, are employed for performance evaluation.

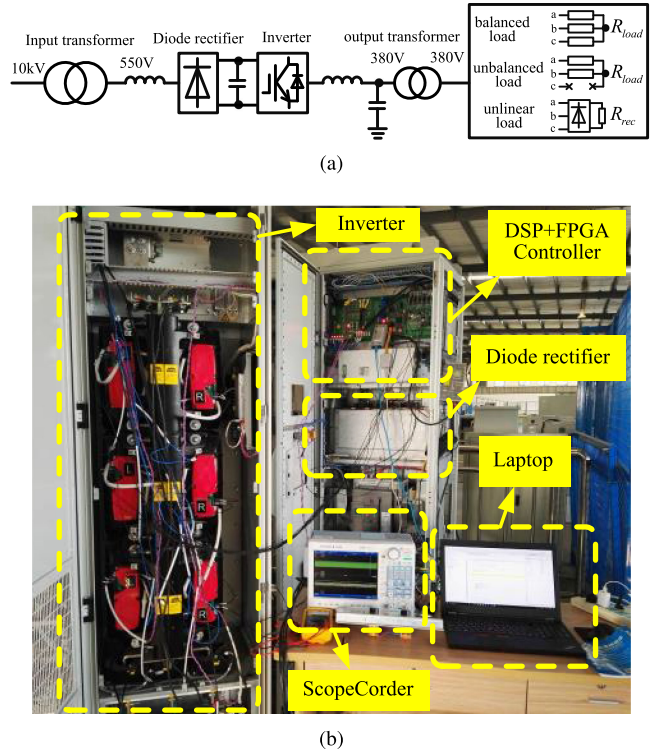
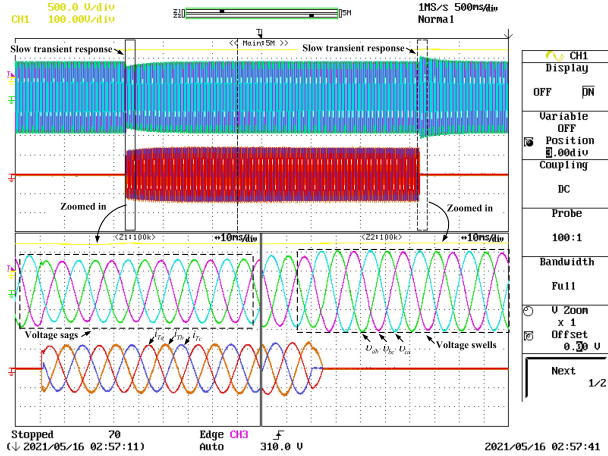


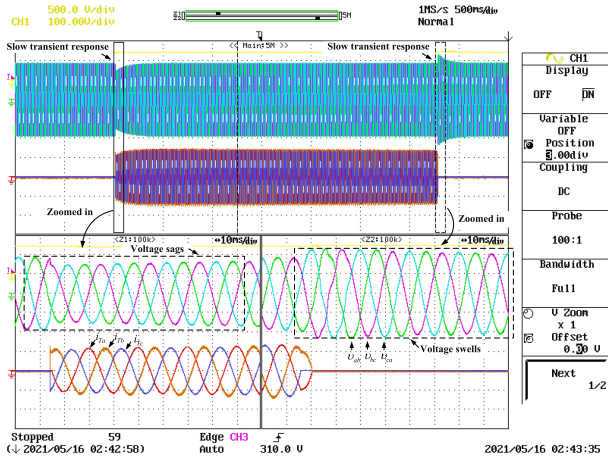
Fig. 13. Experimental setup. (a) Functional block diagram. (b) Photograph.

To begin with, the performance of the converter with three-phase balanced load is investigated. The experimental results are shown in Fig. 14(a)–(c). It can be noted that, for either PR or VPI, when the converter is loaded/unloaded, the output voltage presents a slow transient response. Specifically, the settling time is 300 and 260 ms for PR and VPI, respectively, which can be observed from Fig. 14(a) and (b). The reason for this lies in the constrained loop bandwidth, as addressed in Section IV. This issue is, however, resolved by the developed dRC controller. The experimental result is shown in Fig. 14(c), where it can be appreciated that the output voltage exhibits a fast response with both voltage sags and swells avoided. In the steady state, the output voltage has a negligible difference with either of the three controllers employed, i.e., the magnitude and frequency of the output voltage are 380 V and 50 Hz, respectively (with very limited and negligible fluctuation), and the total harmonic distortion (THD) is less than 0.3%.

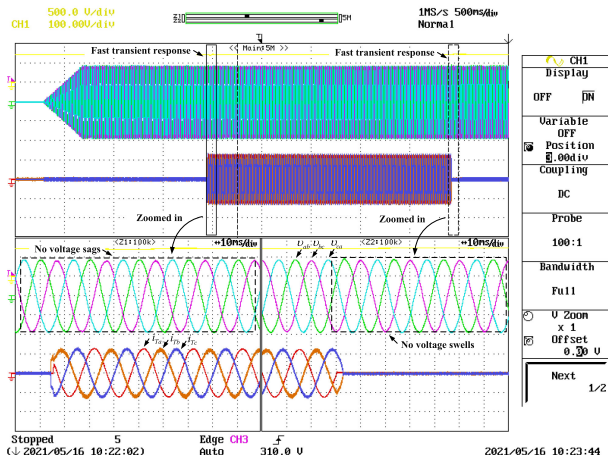
In case of load imbalance, the experimental results are shown in Fig. 15(a)–(c), where PR, VPI, and dRC are employed for voltage regulation, respectively. It can be observed that the output voltages experience an unbalanced feature, i.e., the magnitude of  $v_{ab}$  is lower than that of  $v_{bc}$  and  $v_{ca}$ , during the transient period of time, for both cases of PR and VPI. Also, the performance of PR and VPI is almost the same, as shown in Fig. 15(a) and (b), which is in good agreement with the theoretical findings, as addressed in Fig. 5. However, as shown in Fig. 15(c), with the employment of the developed dRC, the output voltage exhibits a fast transient response, where the unbalanced voltage phenomenon is canceled. Again, the magnitude and frequency of the output voltage in the steady



(a)



(b)

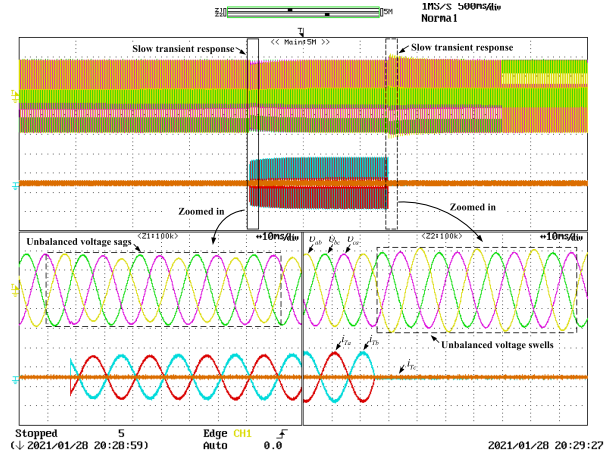


(c)

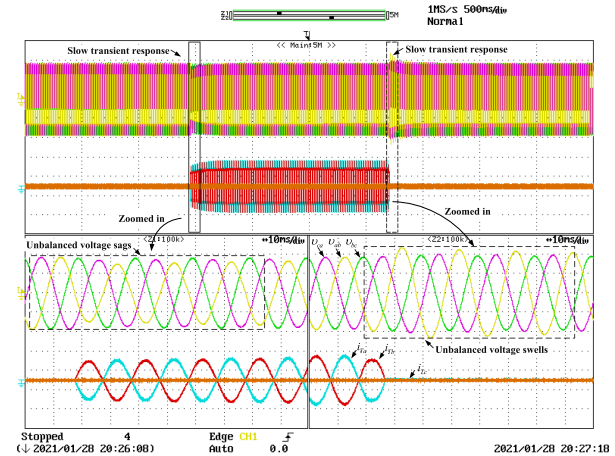
Fig. 14. (a)–(c) Experimental results of the converter with balanced load, where PR, VPI, and the developed dRC controller are employed, respectively.

state are 380 V and 50 Hz, respectively, with either of the three RCs employed. The THD of the output voltage is less than 0.3%.

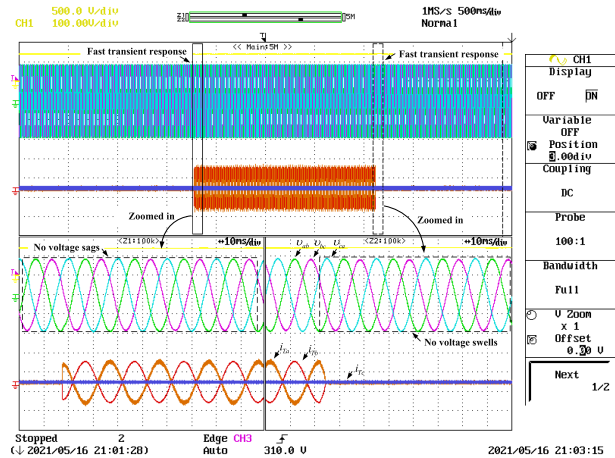
On the other hand, for the case of nonlinear load, the experimental results are shown in Fig. 16. If PR or VPI is employed, the output voltage exhibits a slow transient response, and during the



(a)



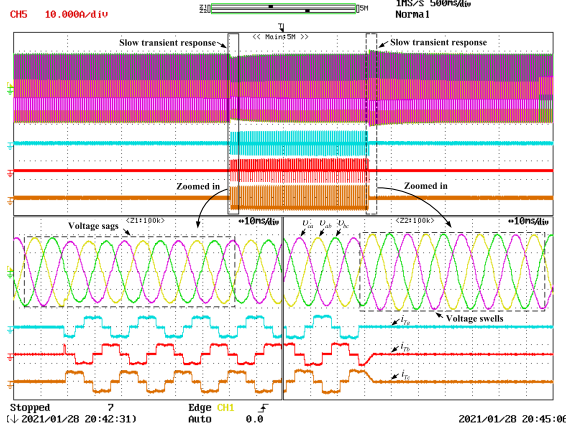
(b)



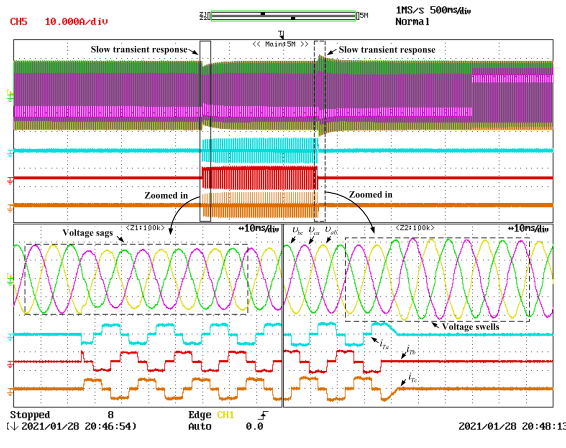
(c)

Fig. 15. (a)–(c) Experimental results of the converter with unbalanced load, where PR, VPI, and the developed dRC controller are employed, respectively.

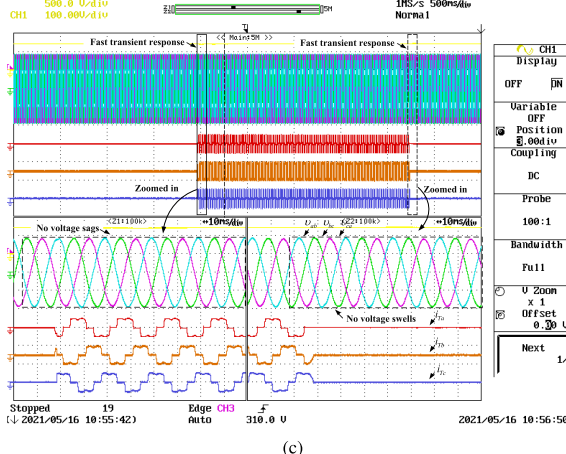
transient period of time, serious distortion of the output voltage can be noted, as shown in Fig. 16(a) and (b). Alternatively, this issue is resolved with the developed dRC, as shown in Fig. 16(c), where the output voltage remains stable when the converter is loaded/unloaded, resulting a high-quality waveform compared



(a)



(b)

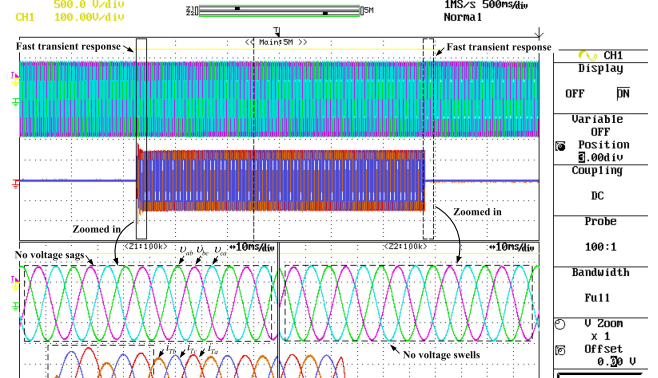


(c)

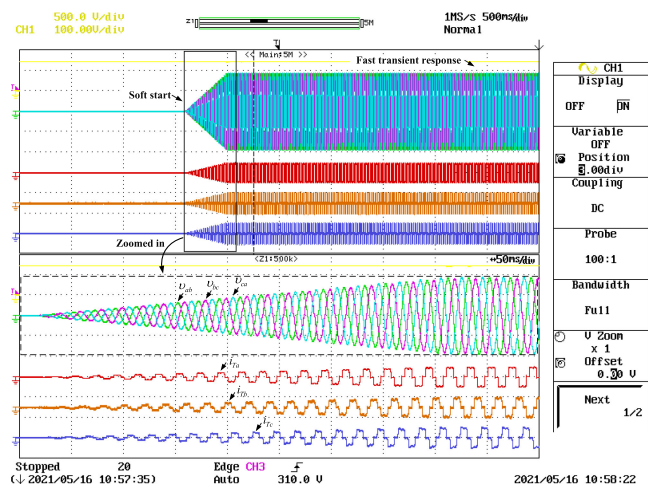
Fig. 16. (a)–(c) Experimental results of the converter with nonlinear load, where PR, VPI, and the developed dRC controller are employed, respectively.

to that of Fig. 16(a) and (b). In the steady state, the THD of the output voltage is less than 0.3% with either of the three controllers employed. However, during the voltage sags and swells, the THD of the voltage can reach 2.2% and 2.3% for PR and VPI, respectively, whereas it is less than 0.5% for dRC.

The experimental result for inductive load is illustrated in Fig. 17(a), where it can be noted that the settling time is about



(a)



(b)

Fig. 17. Experimental results of (a) the converter with inductive load and (b) soft start for voltage buildup of the transformer, where the developed dRC controller is employed.

25 ms before the load current is stable. This is because the decaying dc component, whose amplitude is dependent on the phase of the output voltage when the load is added, appears in the load current. Nevertheless, the voltage is still stable with no voltage sags and swells, and hence, the GFC can still provide high-quality power supply for the load.

It should be noted that a soft start for the voltage buildup of the transformer is designed in the experiment, in order to prevent the transformer excitation inrush current from triggering the instantaneous overcurrent protection of the converter. As shown in Fig. 17(b), where the converter is loaded with nonlinear load, it can be observed that the voltage of the transformer is built in 1 s.

## VI. CONCLUSION

In this article, the dual-loop voltage–current control for GFCs has been thoroughly addressed. The optimum tuning of the inner current loop is investigated to achieve the maximum possible

enhanced active damping based on the developed equivalent plant of the voltage loop. Then, the effectiveness of the existing popular RC for voltage regulation of GFCs has been approached, and the constraints faced by both PR and VPI have been identified. Also, to solve these issues, a dRC is developed to obtain high performance. The above three aspects can be considered as the major contribution of this work.

## APPENDIX

A general pole  $p_{cl}^s$  in the  $s$ -domain can be expressed as

$$p_{cl}^s = a \pm j \cdot b = \omega_0 \cdot \left( -\xi \pm j \cdot \sqrt{1 - \xi^2} \right) \quad (18)$$

where  $a$ ,  $b$ ,  $\omega_0$ , and  $\xi$  are the real part, imagery part, magnitude, and damping ratio of  $p_{cl}^s$ , respectively. It should be mentioned that  $a < 0$  and  $b > 0$  are assumed here, which means that  $p_{cl}^s$  is at the left half part of the  $s$ -plane and is, hence, stable.

Note that  $z = e^{s \cdot T_s}$ , which, upon combined with (18), gives

$$\begin{aligned} p_{cl}^z &= e^{-\xi \cdot \omega_0 \cdot T_s} \cdot \left[ \cos \left( \omega_0 \cdot T_s \cdot \sqrt{1 - \xi^2} \right) \right. \\ &\quad \left. \pm j \cdot \sin \left( \omega_0 \cdot T_s \cdot \sqrt{1 - \xi^2} \right) \right]. \end{aligned} \quad (19)$$

Therefore, the expression for relating the magnitude characteristic of a closed-loop pole in the  $z$ -domain and its correspondence in the  $s$ -domain can be derived from (19), which is given as follows:

$$|p_{cl}^z| = e^{-\xi \cdot \omega_0 \cdot T_s}. \quad (20)$$

Further noting that  $a = -\xi \cdot \omega_0$ , which, combined with (20), yields

$$a = -\xi \cdot \omega_0 = \frac{\ln |p_{cl}^z|}{T_s}. \quad (21)$$

On the other hand, the expression related to the phase characteristic of (19) can be derived as follows:

$$\omega_0 \cdot T_s \cdot \sqrt{1 - \xi^2} = \arctan \left( \frac{\text{Im}(p_{cl}^z)}{\text{Re}(p_{cl}^z)} \right). \quad (22)$$

Finally, the expression related to  $\xi$  can be derived from (21) and (22), which is expressed as follows:

$$\xi = \sqrt{\frac{1}{\left\{ \arctan \left( \frac{\text{Im}(p_{cl}^z)}{\text{Re}(p_{cl}^z)} \right) \cdot \frac{1}{\ln |p_{cl}^z|} \right\}^2 + 1}}. \quad (23)$$

## REFERENCES

- [1] B. Liu, T. Wu, Z. Liu, and J. Liu, "A small-AC-signal injection-based decentralized secondary frequency control for droop-controlled islanded microgrids," *IEEE Trans. Power Electron.*, vol. 35, no. 11, pp. 11634–11651, Nov. 2020.
- [2] P. P. Vergara, M. Salazar, T. T. Mai, P. H. Nguyen, and H. Slootweg, "A comprehensive assessment of PV inverters operating with droop control for overvoltage mitigation in LV distribution networks," *Renewable Energy*, vol. 159, pp. 172–183, Oct. 2020.
- [3] J. Liu, Y. Miura, H. Bevrani, and T. Ise, "A unified modeling method of virtual synchronous generator for multi-operation-mode analyses," *IEEE Trans. Emerg. Sel. Topics Power Electron.*, vol. 9, no. 2, pp. 2394–2409, Apr. 2021.
- [4] M. Pradhan and M. K. Mishra, "Dual  $P$ - $Q$  theory based energy-optimized dynamic voltage restorer for power quality improvement in a distribution system," *IEEE Trans. Ind. Electron.*, vol. 66, no. 4, pp. 2946–2955, Apr. 2019.
- [5] J. Roldán-Pérez, A. García-Cerrada, M. Ochoa-Giménez, and J. L. Zamora-Macho, "Delayed-signal-cancellation-based sag detector for a dynamic voltage restorer in distorted grids," *IEEE Trans. Sustain. Energy*, vol. 10, no. 4, pp. 2015–2027, Oct. 2019.
- [6] Z. Li, Y. Li, P. Wang, H. Zhu, C. Liu, and F. Gao, "Single-loop digital control of high-power 400-Hz ground power unit for airplanes," *IEEE Trans. Ind. Electron.*, vol. 57, no. 2, pp. 532–543, Feb. 2010.
- [7] M. Abarzadeh and K. Al-Haddad, "An improved active-neutral-point-clamped converter with new modulation method for ground power unit application," *IEEE Trans. Ind. Electron.*, vol. 66, no. 1, pp. 203–214, Jan. 2019.
- [8] J. Chen, L.-J. Diao, L. Wang, H. Du, and Z. Liu, "Distributed auxiliary inverter of urban rail train and current control strategy under complicated load condition," *IEEE Trans. Power Electron.*, vol. 31, no. 2, pp. 1745–1756, Feb. 2016.
- [9] J. Chen, L. Wang, L. Diao, H. Du, and Z. Liu, "Distributed auxiliary inverter of urban rail train," *IEEE Trans. Power Electron.*, vol. 31, no. 3, pp. 2518–2529, Mar. 2016.
- [10] R. Razi, H. Iman-Eini, M. Hamzeh, and S. Bacha, "A novel extended impedance-power droop for accurate active and reactive power sharing in a multi-bus microgrid with complex impedances," *IEEE Trans. Smart Grid*, vol. 11, no. 5, pp. 3795–3804, Sep. 2020.
- [11] Y. Han, H. Li, P. Shen, E. A. A. Coelho, and J. M. Guerrero, "Review of active and reactive power sharing strategies in hierarchical controlled microgrids," *IEEE Trans. Power Electron.*, vol. 32, no. 3, pp. 2427–2451, Mar. 2017.
- [12] J. Liu, Y. Miura, and T. Ise, "Cost-function-based microgrid decentralized control of unbalance and harmonics for simultaneous bus voltage compensation and current sharing," *IEEE Trans. Power Electron.*, vol. 34, no. 8, pp. 7397–7410, Aug. 2019.
- [13] B. Adineh, R. Keypour, P. Davari, and F. Blaabjerg, "Review of harmonic mitigation methods in microgrid: From a hierarchical control perspective," *IEEE Trans. Emerg. Sel. Topics Power Electron.*, vol. 9, no. 3, pp. 3044–3060, Jun. 2021.
- [14] X. Xiong, C. Wu, B. Hu, D. Pan, and F. Blaabjerg, "Transient damping method for improving the synchronization stability of virtual synchronous generators," *IEEE Trans. Power Electron.*, vol. 36, no. 7, pp. 7820–7831, Jul. 2021.
- [15] G. Chen and Z. Guo, "Distributed secondary and optimal active power sharing control for islanded microgrids with communication delays," *IEEE Trans. Smart Grid*, vol. 10, no. 2, pp. 2002–2014, Mar. 2019.
- [16] X. Wang, P. C. Loh, and F. Blaabjerg, "Stability analysis and controller synthesis for single-loop voltage-controlled VSIs," *IEEE Trans. Power Electron.*, vol. 32, no. 9, pp. 7394–7404, Sep. 2017.
- [17] Z. Xin, X. Wang, P. C. Loh, and F. Blaabjerg, "Grid-current-feedback control for LCL-filtered grid converters with enhanced stability," *IEEE Trans. Power Electron.*, vol. 32, no. 4, pp. 3216–3228, Apr. 2017.
- [18] M. Shahparasti, M. Mohamadian, A. Yazdian, A. A. Ahmad, and M. Amini, "Derivation of a stationary-frame single-loop controller for three-phase standalone inverter supplying nonlinear loads," *IEEE Trans. Power Electron.*, vol. 29, no. 9, pp. 5063–5071, Sep. 2014.
- [19] P. C. Loh and D. Holmes, "Analysis of multiloop control strategies for LC/LCL-filtered voltage-source and current-source inverters," *IEEE Trans. Ind. Appl.*, vol. 41, no. 2, pp. 644–654, Mar./Apr. 2005.
- [20] A. G. Yepes, A. Vidal, J. Malvar, O. López, and J. Doval-Gandoy, "Tuning method aimed at optimized settling time and overshoot for synchronous proportional-integral current control in electric machines," *IEEE Trans. Power Electron.*, vol. 29, no. 6, pp. 3041–3054, Jun. 2014.
- [21] D. G. Holmes, T. A. Lipo, B. P. McGrath, and W. Y. Kong, "Optimized design of stationary frame three phase AC current regulators," *IEEE Trans. Power Electron.*, vol. 24, no. 11, pp. 2417–2426, Nov. 2009.
- [22] Y. W. Li, "Control and resonance damping of voltage-source and current-source converters with  $LC$  filters," *IEEE Trans. Ind. Electron.*, vol. 56, no. 5, pp. 1511–1521, May 2009.
- [23] M. Zhang, B. Song, and J. Wang, "Circulating current control strategy based on equivalent feeder for parallel inverters in islanded microgrid," *IEEE Trans. Power Syst.*, vol. 34, no. 1, pp. 595–605, Jan. 2019.
- [24] J. Wang and Z. Zhang, "Optimal control parameter design for dual-loop controlled grid-forming VSCs," in *Proc. IEEE/IAS Ind. Commercial Power Syst. Asia*, Weihai, China, Jul. 2020, pp. 1430–1435.

- [25] W. Wu, Y. Liu, Y. He, H. S.-H. Chung, M. Liserre, and F. Blaabjerg, "Damping methods for resonances caused by LCL-filter-based current-controlled grid-tied power inverters: An overview," *IEEE Trans. Ind. Electron.*, vol. 64, no. 9, pp. 7402–7413, Sep. 2017.
- [26] R. Errouissi and A. Al-Durra, "Design of PI controller together with active damping for grid-tied LCL-filter systems using disturbance-observer-based control approach," *IEEE Trans. Ind. Appl.*, vol. 54, no. 4, pp. 3820–3831, Jul./Aug. 2018.
- [27] J. He and Y. W. Li, "Analysis, design, and implementation of virtual impedance for power electronics interfaced distributed generation," *IEEE Trans. Ind. Appl.*, vol. 47, no. 6, pp. 2525–2538, Nov./Dec. 2011.
- [28] J. He, L. Du, B. Liang, Y. Li, and C. Wang, "A coupled virtual impedance for parallel AC/DC converter based power electronics system," *IEEE Trans. Smart Grid*, vol. 10, no. 3, pp. 3387–3400, May 2019.
- [29] A. G. Yépes, F. D. Freijedo, Ó. López, and J. Doval-Gandoy, "Analysis and design of resonant current controllers for voltage-source converters by means of Nyquist diagrams and sensitivity function," *IEEE Trans. Ind. Electron.*, vol. 58, no. 11, pp. 5231–5250, Nov. 2011.
- [30] C. Lascu, L. Asiminoaei, I. Boldea, and F. Blaabjerg, "Frequency response analysis of current controllers for selective harmonic compensation in active power filters," *IEEE Trans. Ind. Electron.*, vol. 56, no. 2, pp. 337–347, Feb. 2009.
- [31] L. Zheng, F. Jiang, J. Song, Y. Gao, and M. Tian, "A discrete-time repetitive sliding mode control for voltage source inverters," *IEEE Trans. Emerg. Sel. Topics Power Electron.*, vol. 6, no. 3, pp. 1553–1566, Sep. 2018.
- [32] G. A. Ramos, R. I. Ruget, and R. Costa-Castelló, "Robust repetitive control of power inverters for standalone operation in DG systems," *IEEE Trans. Energy Convers.*, vol. 35, no. 1, pp. 237–247, Mar. 2020.
- [33] R. Turner, S. Walton, and R. Duke, "Robust high-performance inverter control using discrete direct-design pole placement," *IEEE Trans. Ind. Electron.*, vol. 58, no. 1, pp. 348–357, Jan. 2011.
- [34] U. Jensen, F. Blaabjerg, and J. Pedersen, "A new control method for 400-Hz ground power units for airplanes," *IEEE Trans. Ind. Appl.*, vol. 36, no. 1, pp. 180–187, Jan./Feb. 2000.
- [35] H. Kim, M. W. Degner, J. M. Guerrero, F. Briz, and R. D. Lorenz, "Discrete-time current regulator design for AC machine drives," *IEEE Trans. Ind. Appl.*, vol. 46, no. 4, pp. 1425–1435, Jul./Aug. 2010.
- [36] D. Pérez-Estévez, J. Doval-Gandoy, A. G. Yépes, Ó. López, and F. Baneira, "Enhanced resonant current controller for grid-connected converters with LCL filter," *IEEE Trans. Power Electron.*, vol. 33, no. 5, pp. 3765–3778, May 2018.
- [37] A. G. Yépes, F. D. Freijedo, J. Doval-Gandoy, Ó. López, J. Malvar, and P. Fernández-Comesaña, "Effects of discretization methods on the performance of resonant controllers," *IEEE Trans. Power Electron.*, vol. 25, no. 7, pp. 1692–1712, Jul. 2010.
- [38] D. Pérez-Estévez, J. Doval-Gandoy, A. G. Yépes, and Ó. López, "Positive- and negative-sequence current controller with direct discrete-time pole placement for grid-tied converters with LCL filter," *IEEE Trans. Power Electron.*, vol. 32, no. 9, pp. 7207–7221, Sep. 2017.
- [39] M. M. Ghaderijani, A. Camacho, C. Moreira, M. Castilla, and L. García de Vicuña, "Imbalance-voltage mitigation in an inverter-based distributed generation system using a minimum current-based control strategy," *IEEE Trans. Power Del.*, vol. 35, no. 3, pp. 1399–1409, Jun. 2020.

**Zhihong Zhao** (Member, IEEE) received the B.S. degree in electric engineering and automation from the China University of Petroleum, Qingdao, China, in 2008, and the M.S. and Ph.D. degrees in electric power engineering from Southeast University, Nanjing, China, in 2011 and 2017, respectively.

In 2017, he joined the Department of Electrical Engineering, School of Automation, Nanjing University of Science and Technology, Nanjing. His research interests include current control of grid-connected converters, active damping of *LCL* filter resonance, stability enhancement for parallel-connected converters, current control of converters in a weak grid, and virtual synchronous generator control.

**Zhichao Sun** received the B.S. degree in automation engineering from the Nanjing Institute of Technology, Nanjing, China, in 2017. He is currently working toward the M.E. degree in power electronics and power transmission with the Nanjing University of Science and Technology, Nanjing.

His research interests include switched-mode power supply and control of converters.

**Yilong Feng** received the B.S. degree in electrical engineering and automation from the Henan University of Science and Technology, Luoyang, China, in 2020. He is currently working toward the M.E. degree in electrical engineering with the Nanjing University of Science and Technology, Nanjing, China.

His research interests include multiconverter parallel system stability.

**Baojian Ji** received the B.S. degree in automation engineering from Nanjing Normal University, Nanjing, China, in 2002, the M.S. degree in electrical engineering from the Nanjing University of Aeronautics and Astronautics, Nanjing, in 2007, and the Ph.D. degree from Southeast University, Nanjing, in 2012.

In 2017, he was an Associate Professor with Nanjing Tech University, Nanjing, where he was also the Head of the Department of Electrical Engineering. In 2018, he joined the Nanjing University of Science and Technology, Nanjing, as an Associate Professor. His research interests include the digital control technique and the development of grid-tied inverters for renewable energy.

**Shuzheng Wang** received the Ph.D. degree in electrical engineering from Southeast University, Nanjing, China, in 2015.

He is currently an Associate Professor with the Jiangsu Province Intelligent Distribution Network Technology and Equipment Collaborative Innovation Center, Nanjing Institute of Technology, Nanjing. His current research interests include high-power multilevel converter technology, photovoltaic grid-connected technology, power quality assessment and management, flexible dc transmission, and distribution technology.

**Jianfeng Zhao** received the B.S. degree in electrical engineering from the Huainan Mining Institute, Anhui, China, in 1995, the M.S. degree in automation from the Nanjing University of Aeronautics and Astronautics, Nanjing, China, in 1998, and the Ph.D. degree in electrical engineering from Southeast University, Nanjing, in 2001.

In 2001, he joined the Faculty of the School of Electrical Engineering, Southeast University, where he has been a Professor since 2008 and has been teaching and researching in high-power electronics. Since 2014, he has been the President of the School of Electrical Engineering, Southeast University. He has authored more than 80 technical papers. He holds 35 Chinese patents. His current research interests include utility applications of power electronics in smart grids, such as solid-state transformers, active filters for power conditioning, flexible ac transmission system devices, multilevel ac motor drivers, and efficient energy utilization.

Dr. Zhao has been a member of the Technical Committee of Standard Voltages, Current Ratings and Frequencies of China since 2010 and the All-China Youth Federation since 2010.